INTERFACE

royalsocietypublishing.org/journal/rsif

Research

Cite this article: Zhang B, Anderson PSL. 2022 Modelling biological puncture: a mathematical framework for determining the energetics and scaling. *J. R. Soc. Interface* **19**: 20220559.
https://doi.org/10.1098/rsif.2022.0559

Received: 2 August 2022
Accepted: 26 September 2022

Subject Category:
Life Sciences–Physics interface

Subject Areas:
biomechanics, biophysics

Keywords:
puncture, energy, scaling, fracture

Author for correspondence:
Bingyang Zhang
e-mail: bzhang53@illinois.edu

Electronic supplementary material is available online at https://doi.org/10.6084/m9.figshare.c.6238488.

THE ROYAL SOCIETY PUBLISHING

Modelling biological puncture: a mathematical framework for determining the energetics and scaling

Bingyang Zhang and Philip S. L. Anderson

School of Integrative Biology, University of Illinois Urbana-Champaign, Urbana, IL 61801, USA

BZ, 0000-0003-2138-1191; PSLA, 0000-0001-7133-8322

Biological puncture systems use a diversity of morphological tools (stingers, teeth, spines etc.) to penetrate target tissues for a variety of functions (prey capture, defence, reproduction). These systems are united by a set of underlying physical rules which dictate their mechanics. While previous studies have illustrated form–function relationships in individual systems, these underlying rules have not been formalized. We present a mathematical model for biological puncture events based on energy balance that allows for the derivation of analytical scaling relations between energy expenditure and shape, size and material response. The model identifies three necessary energy contributions during puncture: fracture creation, elastic deformation of the material and overcoming friction during penetration. The theoretical predictions are verified using finite-element analyses and experimental tests. Comparison between different scaling relationships leads to a ratio of released fracture energy and deformation energy contributions acting as a measure of puncture efficiency for a system that incorporates both tool shape and material response. The model represents a framework for exploring the diversity of biological puncture systems in a rigorous fashion and allows future work to examine how fundamental physical laws influence the evolution of these systems.

1. Introduction

Biological organisms use a variety of morphological elements, including teeth [1–5], claws [3,6], spines [7–9] and stingers [10,11], to puncture a wide range of target materials or tissues [12]. Puncture is defined here as the use of a morphological tool to initiate fracture in a material, followed by the tool penetrating the material and propagating the fracture [12]. This biological puncture is used for several functions including prey capture [2,8,13], defence [7,8] and reproduction [14]. While extremely diverse in materials, scale and functions [3,12,15], biological puncture systems are united by the underlying mechanics of puncture, which should lead to certain shared fundamental morphological and mechanical similarities [12,15]. For example, most organic puncture tools exhibit a tapered shape that diminishes in cross-sectional size towards a fixed tip radius. Furthermore, all puncture incorporates fracture initiation and propagation—an energy-driven, material-dependent failure process. While these commonalities have been identified previously, there have been few attempts to formalize how variables such as shape or size quantitatively influence biological puncture performance using mathematical modelling or scaling [3]. Here, we present an idealized mathematical model for biological puncture events based on energy expenditure that allows for both analytical solutions of energy components and derived scaling relationships between energetics and puncture performance. This analytical model highlights the commonalities across puncture systems; shedding light on the physics underlying biological puncture and providing a promising avenue for understanding how biomechanical principles influence evolutionary convergence.

Biological puncture is a complex interplay between various mechanical processes. A successful puncture event depends on puncture tool morphology,

target material properties, and the governing contact mechanics and dynamics. One predominant factor that connects all of these is the energy associated with puncture. As suggested by previous studies on puncture energetics [5,12], the energy flow/balance between the puncturing organism and its target may be a crucial principle for determining biological puncture performance. One could hypothesize that evolution would favour puncturing organisms that maximize energy transformation into creating fracture while minimizing energy lost to material deformation and penetration resistance from friction. Such natural demand for higher energy efficiency should significantly influence puncture tool shape depending on the target material properties. A sharper tool requires less fracture energy to puncture due to a higher stress/strain energy density concentration [12,16] and produces less material deformation because of its smaller volume to accommodate [12,17]. This sort of relationship between morphology and required energy/force in puncture has been reported in many biological systems such as viper fangs [4], cactus spines [7], mammalian canine teeth [1,18] and medical needle insertion [19,20]. However, these findings from the literature regarding puncture energetics lack generalization. A knowledge gap remains between puncture tool shape and material characterization and how their effects quantitatively impact puncture energy response. For this reason, we aim to establish a theoretical framework formalizing the idea of energy balance in puncture into a mathematical model, allowing for the energetics of specific puncture systems to be biomechanically contextualized.

Since the early work by Stevenson & Maleck [21], there have been a limited number of theoretical investigations and modelling attempts on puncture mechanics in soft solids and bio-tissues [16,20,22–26]. These studies often focus on specific puncture cases where damage is produced by either a flat punch or a cylindrical-like tool [16,20,22,26] and are mostly related to medical needle injection [20,22,23] and material characterization [16,24,25]. However, biological puncture tools such as teeth [1], fangs [4] and stingers [15] often resemble tapered, conical shapes, at least at their tips. In this manuscript, we explore a general biomechanical puncture scenario where a conical puncture tool dynamically impacts and generates fracture in a hyperelastic soft material using mathematical tools including continuum mechanics and fracture mechanics.

In addition to creating a quantitative baseline for puncture energetics, this model should also provide insights into the scaling of biological puncture. Little in organismal biology makes sense without the context of scale [27], and it has been shown that characteristic length scales of a puncture system can play a critical role in determining the amount of energy necessary for puncture [3,4,12,15,17,19,20,22,23,25,28]. Furthermore, characteristic length scales identified in engineered systems are reflected in biology, including puncture tool dimensions related to sharpness [4,19,23,25], the overall size of an organism [3,12], and contact area or volume associated with puncture as functions of depth of puncture [15,17,20,22,28]. It is not fully understood how mechanical energy flow between puncture tool and target is influenced by these length scales. The model presented here will provide a theoretical approach to identify physical length scales underlying the mechanical processes involved in puncture and quantify scaling relationships between length scale and puncture energy.

This manuscript begins with a systematic, mathematical description of the kinematics and fracture mechanics underlying biological puncture focusing on penetration after the initial fracture for reasons discussed below. Analytical solutions for three energy components associated with puncture (stored strain energy, frictional work and work to fracture), as well as their corresponding scaling relationships with depth of puncture (our characteristic length scale) are established through theoretical modelling. Numerical and experimental verification are carried out via finite-element (FE) simulations and dynamic puncture tests to quantitatively verify the proposed puncture damage morphology and scaling relationships. Finally, we discuss the potential applications of the theory in developing an energy ratio as a new performance metric for biological puncture as well as further implications for better understanding the effect of friction on puncture biomechanics and generalization of scaling in biological puncture systems.

2. Theory

In this section, we introduce and model kinematics and mechanical processes underlying puncture and identify required energy components contributing to frictional dissipation, fracture and elastic deformation. We use this model to derive scaling relations between quantities governing the energetics of puncture and necessary physical length scales for failure in the context of solid mechanics and fracture mechanics in highly deformable tissues and soft materials, while making reasonable assumptions within the scope of biological reality.

2.1. Kinematics of impact-induced puncture

To describe the energy balance involved in dynamic puncture, we consider a scenario as illustrated in figure 1: puncture fracture occurs when a sharp, hard projectile having a mass, m_0, and an initial velocity, v_0, impacts and penetrates a soft stationary target material having a mass, m_1. Note that this model focuses on the penetration of the tool into the target, namely, the propagation of the fracture post fracture initiation. While the force/energy required to initiate fracture at the start of puncture will be of vital importance to biological puncture systems, we focus on the penetration phase here for two reasons: (i) our primary interests in this model are the energy balance and the scaling relationships between puncture energies and shape, size and material response, making the self-similar penetration phase the focus; (ii) it is challenging to predict the exact onset of fracture without knowing additional information about the material properties and fracture process [29]. We are taking a cue from the Griffith equation for fracture mechanics [30,31] which assumes a crack already exists and determines how scale and energy relate to expanding the crack. Future theoretical and experimental work will hopefully be able to incorporate variation in tip geometry and fracture initiation into this framework.

In nature, the relative motion of the puncturing organism and its target often depends on their interactions and relative masses. Therefore, to simplify the problem, we make the following initial assumptions to describe general boundary conditions that could be extended to realistic biological puncture scenarios:

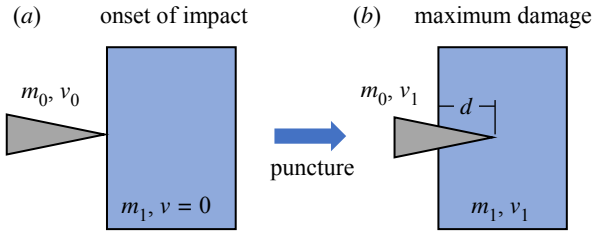

Figure 1. Schematics of dynamic puncture. (*a*) The states (masses (m) and speeds (v)) of the projectile and the target material at the onset of impact ($m_1 \gg m_0$). The target material is initially stationary ($v = 0$). (*b*) The projectile and the target material reach the same speed ($v_1 \approx 0$) at the maximum depth of puncture.

(i) Both the projectile and target material are free of constraints from the surrounding environment.
(ii) No post-contact separation between the projectile and target material occurs until the maximum depth of puncture is reached.
(iii) Friction between the target material and the ground is negligible compared with the puncture force.

The conservation of momentum requires

$$m_0 v_0 = (m_0 + m_1) v_1, \tag{2.1}$$

where v_1 is the final velocity of either the target material or puncture tool when the depth of puncture reaches its maximum, d (figure 1). The loss of kinetic energy during puncture fracture process is

$$\begin{aligned} \Delta E_k &= E_{k,0} - E_{k,1} \\ &= \frac{1}{2} m_0 v_0^2 - \frac{1}{2}(m_0 + m_1) v_1^2. \end{aligned} \tag{2.2}$$

Substituting equation (2.1) yields

$$\Delta E_k = \frac{m_1}{m_0 + m_1} \cdot \frac{1}{2} m_0 v_0^2 \equiv K E_{k,0}, \tag{2.3}$$

where $E_{k,0}$ and $E_{k,1}$ are total kinetic energies of the system before and after puncture damage. When $m_1 \gg m_0$, the prefactor $K = m_1/(m_0 + m_1) \to 1$, and $\Delta E_k \approx E_{k,0}$. In this particular case, where the target mass is far larger than that of the puncture tool, all initial kinetic energy is converted into other forms at the maximum depth of puncture. This limit is energetically equivalent and may be applied to a puncture event where the target is completely fixed and its movement restrained.

While in general, $\Delta E_k < E_{k,0}$, it should be pointed out that other forms of constraints may exist in realistic puncture systems. For example, in the presence of an external load applied on the target material, the conservation of momentum (equation (2.1)) may no longer hold due to the associated work done. In this case, the loss of kinetic energy due to puncture, ΔE_k, can be estimated through the expression $\Delta E_k = E_{k,0} - E_{k,1} + U_w$, where $E_{k,0}$ and $E_{k,1}$ are experimentally measurable through speed and mass characterization, and U_w can be determined via the work done by the applied load to change the system's kinetic energy. Moreover, we note that with a predetermined ΔE_k value, the local puncture energy conversion is largely dependent on the properties of the projectile and the target material as we elaborate in the puncture theory in the following sections. This process is unlikely to be affected by applied constraints for the case we are interested in where the material substrate is extremely large, and the boundary effect and the effect of constraint-induced internal fields are negligible.

This lost kinetic energy, ΔE_k, becomes the source of energy for propagating puncture in the target material. Specifically, it is converted into three energy contributions

$$\Delta E_k = W + \Delta U_{\mathrm{el}} + W_f, \tag{2.4}$$

where W is the total released fracture energy in forms of fracture surface energy and bulk dissipative energy [32]; ΔU_{el} is the change of stored strain energy in the target material due to elastic deformation; and W_f is the work done due to interfacial friction between the projectile and the target material. These three energy components represent three different energy criteria required to propagate biological puncture: creating the actual cut or opening in the target tissue, deforming the tissue and pushing it out of the way during insertion of the tooth/spine/stinger, and overcoming friction between said tooth/spine/stinger and the surrounding tissue it is sliding past. Particularly, complex biological substrate materials often exhibit other internal resistance to puncture such as viscoelasticity induced bulk energy dissipation. However, as we point out above and further discuss in §2.2.3, this energy contribution is generally considered as part of the total released fracture energy, W. Quantification of the bulk dissipation arising from nonlinear viscoelasticity and other rate-dependent effects in soft polymers and biological materials is beyond the scope of this study. For the following discussion, we select ideal, simplified model materials with low viscoelastic and other rate-dependent effects, where the bulk energy dissipation can be neglected.

In light of established theoretical [16,23,24,33] and experimental [5,7,17,19,34] models for soft fracture incorporating contact mechanics, we solve the energy balance equation of puncture (equation (2.4)) and establish scaling relations for each energy component in the following sections. The theoretical predictions reveal the significant roles played by both morphology and material mechanical response in determining the governing puncture energetics.

2.2. Scaling relations for energy components

2.2.1. Description of ductile puncture failure

To quantify scaling relations between the three components of ΔE_k (equation (2.4)) and necessary physical length scales associated with puncture, we consider an ideal puncture configuration: a conical-shaped puncture tool, with cusp angle 2θ, penetrates the surface of a soft, highly deformable target material by a depth of puncture, d (as illustrated in figure 2). The target material is subjected to a finite elastic indentation due to the reaction force. The depth of indentation, d_e, is measured from the unconstrained surface to the first point of contact (figure 2). To estimate the effects of tool geometries and material response on puncture energy components, we make the following key assumptions:

— The puncture tool is sharp and has a radius of curvature, r_{tip}, at the tip that satisfies $r_{\mathrm{tip}} \ll d$.
— The overall size/length scale of the target material satisfies $\ell \gg d \gg r_{\mathrm{tip}}$ (i.e. a half-space).
— The puncture tool can be treated as rigid compared with the stiffness and deformablity of the target material.

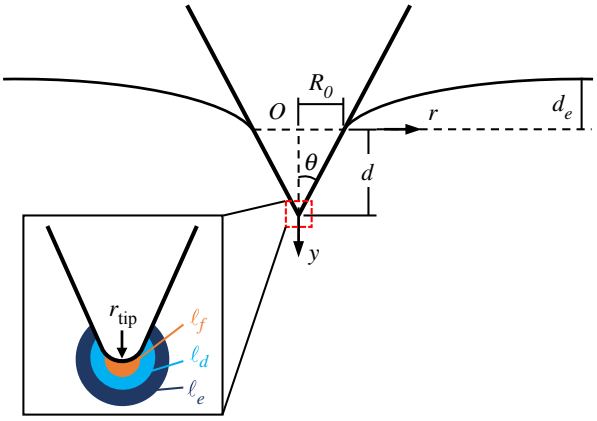

Figure 2. Schematics of puncture tool configuration and associated material deformation at the maximum depth of puncture, d. The reaction force in y-direction causes an elastic indentation of depth d_e. Subfigure: The local material response for ductile puncture failure transitions from a linear elastic regime to nonlinear, fracture-relevant regimes as the puncture tool tip is approached. The characteristic length scales associated with the local failure process at the puncture tool tip are highlighted in different colours: elasto-fracture length, ℓ_e (dark blue); dissipative length, ℓ_d (light blue); damage zone size, ℓ_f (orange).

— For soft, biological systems, it is reasonable to describe the constitutive response of the target material using hyperelasticity.
— To demonstrate the full physical picture of puncture energetics, as a starting point, we assume an ideal model material having the neo-Hookean constitutive response with low viscoelastic and rate-dependent effects. Under such simplification, the bulk dissipative energy contribution is neglected.

Similar to conventional far-field failure and other failure mechanisms involving contact mechanics (e.g. cutting) in soft materials [32,33], near-tip stress/strain concentration is expected in puncture. To better understand and account for the energy contributions directly from the local failure process caused by a sharp puncture tool tip in our selected material model above, here we limit our scope to discuss the fracture-relevant physical length scales near the puncture tool tip. The material response during puncture transitions from a purely elastic regime to nonlinearity-dominated regimes incorporating large-deformation, fracture-related dissipation, and eventually local failure process as the puncture tool tip is approached. The onsets of these critical transitions can be approximated using standard characteristic length scales for soft fracture [31–33], as illustrated in figure 2:

(i) large-deformation zone size, ℓ_e, at which length scale the material transitions from linear elasticity to nonlinear elasticity;
(ii) dissipation zone size, ℓ_d, at which the macroscopic mechanical field is transferred to failure process and irreversible dissipation sets in (note there is no general one-to-one correspondence between ℓ_d and the length scale associated with the bulk dissipation because the former defines a localized process while the latter depends on the global mechanical field [32]);
(iii) damage zone size, ℓ_f, marking the onset of the local failure process (e.g. chain breakage) in the vicinity of the crack tip.

These characteristic regions are necessary to sustain the failure propagation caused by the puncture tool tip. The relative magnitude of their length scales are determined by the material properties and the type of failure that occurs [32]. We argue based on contact-driven failure mechanisms [33] that in highly deformable, soft materials subjected to a puncture tool whose tip radius is sufficiently small (i.e. $r_{tip} \lesssim \ell_f$), puncture fracture can be characterized by soft, ductile failure behaviours that incorporate small-scale-yield-like conditions similar to those found in cutting fracture [33]. The effects of nonlinearity near the crack tip are minimized, and the characteristic length scales largely overlap (i.e. $r_{tip} \lesssim \ell_f \lesssim \ell_d \lesssim \ell_e$). Evidence for the above hypothesis from cutting failure and further discussion of the fracture-relevant characteristic length scales are provided in the electronic supplementary material. Briefly, to establish simple scaling relationships based on equation (2.4), we implement a puncture tool with an extremely small tip radius below the critical length scale for fracture. The following assumptions stem from the resultant small-scale-yield-like condition:

— The local dissipative contribution at the puncture tool tip to the total failure energy W is negligible.
— The large deformation zone associated with the failure caused by the puncture tool tip is extremely small, and its contribution to ΔU_{el} is minor compared with that from the material displaced to accommodate the puncture cone body farther away from the puncture tool tip.

Now we use this framework to derive the scaling relations of the three energy components in our model: friction, fracture and deformation.

2.2.2. Frictional work

The friction forces that resist fracture propagation during puncture are assumed to increase linearly with the instantaneous contact area from zero to a maximum value at d. Thus, the work done to overcome this friction has a form

$$W_f = \int_0^d A(y) f \cos\theta \, dy, \tag{2.5}$$

where $A(y)$ is the contact area between the cone and material when penetration reaches a depth y ($0 \le y \le d$), and f is the average friction force per unit contact area. $A(y)$ can be expressed in terms of θ

$$A(y) = \pi y^2 \frac{\sin\theta}{\cos^2\theta}. \tag{2.6}$$

Substituting equation (2.6) into equation (2.5) gives

$$W_f = \frac{\pi}{3} \tan\theta f d^3. \tag{2.7}$$

The implicit assumption in equation (2.7) is that f is approximately a constant interfacial property, e.g. at a relatively large depth of puncture, d. Support for this assumption is discussed in §4.2. Equation (2.7) implies that W_f scales with the volume of the material that has been displaced by the puncture tool, i.e.

$$W_f \sim d^3. \tag{2.8}$$

Moreover, it appears, based on equation (2.7), that for the same d, a smaller 2θ value leads to less frictional contribution. This speculation agrees with findings in biological puncture with a slender tool [15].

2.2.3. Released fracture energy

To estimate the energy required to create new fracture surfaces W, we must first describe the morphology of the damage caused by a conical puncture tool. The conical puncture problem starts with axisymmetric elastic indentation. However, such axial symmetry is not necessarily retained during the following initiation and propagation of the fracture. Although the formation of multiple crack fronts across the tool-material interface is possible in an idealized, homogeneous material or at extremely high strain rates [35], we hypothesize that in our selected model materials (i.e. neo-Hookean-like soft polymers), within our range of puncture rates of interest (less than 100 m s^{-1}), a symmetric breaking effect caused by the imperfections and defects in the material or on the puncture tool is more likely to occur during puncture testing. This ultimately leads to a preferred fracture plane and the formation of a planar triangular crack (in the undeformed state, as illustrated in figure 3*a*,*c*). A superficial crack having a size $2a_0$ remaining where the tool first enters the material (figure 3*a*). Evidence for such damage morphology is provided in §3.1 through experimental visualization.

In general, W can be approximated by integrating the critical strain energy release rate G_c over the area of the proposed fracture surface A_{frac}, where G_c can be expressed as, for a planar crack [31,32],

$$G_c = \Gamma + \Gamma_d, \tag{2.9}$$

where Γ is the mode-I material toughness/minimal fracture energy and Γ_d is the bulk dissipative contribution. The estimation of G_c using experimentally measurable apparent fracture energy is largely testing condition dependent. For simplicity, here we invoke the ideal model material assumption and the small-scale-yield-like condition (§2.2.1) and assume low bulk dissipative contribution, Γ_d. Therefore, $G_c \sim \Gamma$, and

$$W \sim \int_{A_{\text{frac}}} \Gamma \, \mathrm{d}A = \tan\theta' \Gamma d^2, \tag{2.10}$$

where θ' denotes the half taper angle of the residual fracture surface (figure 3*c*).

Additionally, to complete the physical picture, we make the following morphological assumption based on experimentally evident material responses: the relative size of the planar crack satisfies

$$r_{\text{tip}} \ll a_0 < R_0, \tag{2.11}$$

where R_0 is the radial size of the puncture tool at a distance d from the tip (figure 2). The above condition is the result of a two-step fracture growth process in conical puncture in a highly deformable, hyperelastic material: the initial mode-I fracture occurring at the tip having a length scale, r_{tip}, followed by the inflation and further expansion of the fracture to a radius $R(y)$ to accommodate the radial size of the cone at y. Note, because r_{tip} is extremely small, the expansion of the puncture cavity in the radial direction is governed by a combination of elastic deformation and mode-I fracture

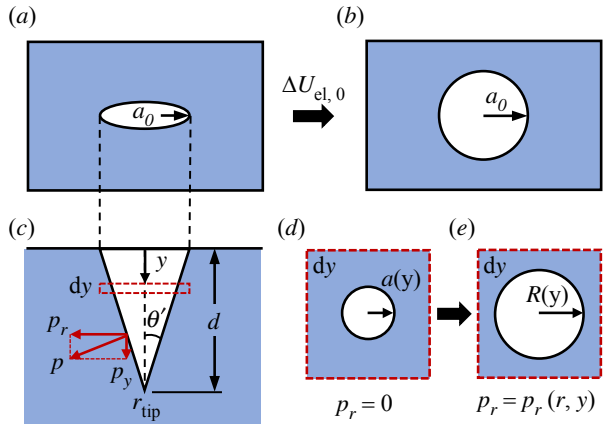

Figure 3. Puncture fracture surface morphology. (*a*) View of the residual superficial crack having size a_0 on the impact surface of the material. (*b*) The planar crack from (*a*) becomes inflated into a circular hole of the same radial size under an elastic energy expenditure, $\Delta U_{\text{el},0}$. (*c*) Cross-sectional view of the fracture surface (either in the initial undeformed configuration (*a*) or the opened state (*b*)). The dotted red rectangle illustrates the infinitesimal slice of the cavity referenced in (*d*) and (*e*). (*d*,*e*) Further elastic radial expansion of the opened cavity within an infinitesimal slice, dy, can be approximated to planar deformation of a circular hole from radius $a(y)$ to $R(y)$ under an inflating pressure p_r applied on the cavity wall.

propagation on the preferred fracture plane. Consequently, when the puncture tool is removed, only the reversible elastic deformation recovers and the irreversible damage having radial size $a(y) = a_0 - \tan\theta' y$ remains at y, resulting in a triangular undeformed crack. It was experimentally reported [28,36] that the residual damage size is significantly smaller than the size necessary to accommodate the puncture tool in a highly stretchable, neo-Hookean-like silicone rubber throughout the puncture depth, which supports $a(y) < R(y)$ and thus the second part of condition (2.11). However, a larger magnitude of $a(y)$ than $R(y)$ was observed in a more brittle silicone rubber [28,36], presumably due to lateral cracking and branching. These observations necessitate the implementation of a material model associated with ductile failure (e.g. the neo-Hookean model) to restrict the growth of the planar crack to be no larger than the radial tool size. Further investigation on the elastic expansion contributing to ΔU_{el} is carried out in §2.2.4.

Equation (2.10) implies that W scales with d^2, or equivalently, surface area. The ramifications of this scaling relation have been noted in a review on biological puncture systems [12]. It was noted that smaller biological puncture systems tend to have faster puncture speeds [6,37,38], and it was suggested that this was partly due to the kinetic energy available for puncture (which scales with mass/volume) reducing faster with body size than the energy required to create damage (which scales with surface area). Higher speeds are necessary to compensate for the discrepancy and maintain the puncture performance across scales.

2.2.4. Stored elastic energy

The elastic contribution to ΔE_k, ΔU_{el}, represents energy used to deform the material. It can be approximated as the superposition of two components:

(i) the elastic deformation due to indentation (i.e. d_e);

Table 1. Energy comparison between three-dimensional puncture damage simulations and theoretical predictions at different tool cusp angles.

2θ [°]	d_{nom} [mm]	$2\theta'$ [°]	$\frac{W}{\mu d^3}$ (FE)	$\frac{W}{\mu d^3}$ (theory)	$\frac{\Delta U_{el}}{\mu d^3}$ (FE)	$\frac{\Delta U_{el}}{\mu d^3}$ (theory)*	$\frac{\Delta U_{el,0}}{\mu d^3}$	$\frac{W}{\Delta E_k}$ (FE)	$\frac{W}{\Delta E_k}$ (theory)
30	4.7	11.0	2.6×10^{-2}	2.0×10^{-2}	0.10	0.09	9.0×10^{-3}	0.202	0.184
40	4.7	14.7	4.0×10^{-2}	2.7×10^{-2}	0.19	0.18	1.6×10^{-2}	0.175	0.133
50	4.5	18.0	5.8×10^{-2}	3.5×10^{-2}	0.32	0.32	2.4×10^{-2}	0.153	0.098
60	4.3	23.0	8.7×10^{-2}	4.7×10^{-2}	0.50	0.50	4.0×10^{-2}	0.147	0.085

* ΔU_{el} includes the contribution of $\Delta U_{el,0}$.

(ii) the opening and further elastic expansion of the undeformed puncture fracture surface to accommodate the puncture tool size.

The first component is expected to be minor compared with the magnitude of the second for a very soft material or a sharp puncture tool with a small cusp angle producing a small indentation force. We show this in §3.2.1 via FE simulations. Therefore, to determine the scaling relation for ΔU_{el}, we focus on the effect of the second component.

To derive a closed-form expression for ΔU_{el}, we assume that the elastic expansion of the undeformed puncture fracture surface to the size of the puncture tool can be reproduced by a two-step process: (i) the planar triangular crack is opened into a conical cavity having the same radial size under an initial pressure or surface traction, p_0; and (ii) an additional changing inflating pressure, p, is then applied axisymmetrically and perpendicularly on the circular cavity wall (figure 3) such that no bending of the wall surface occurs, and the taper angle increases from $2\theta'$ to 2θ.

We denote the elastic energy required for the first step as $\Delta U_{el,0}$ (figure 3). To estimate the magnitude of $\Delta U_{el,0}$, we adopt an approach similar to the one proposed by Shergold and Fleck for a cylindrical punch [22,26]. We introduce a dimensionless function $f(a/R)$ to describe the normalized elastic energy associated with a symmetric problem where a planar crack having length $2a$ in an elastic substrate is wedge opened by a rigid circle having radius R under *plane strain* (electronic supplementary material, figure S3). Therefore, $\Delta U_{el,0}$ can be expressed as

$$\Delta U_{el,0} = \int_0^d \mu a(y)^2 f(1)\,dy = \frac{1}{3}\tan^2\theta' \mu f(1) d^3 \equiv k_0 \mu\, d^3, \tag{2.12}$$

where the prefactor k_0 is dimensionless. We determine the explicit value of $f(1)$ to be $f(1) \approx 2.91$ using a two-dimensional symmetric FE method as detailed in electronic supplementary material, S4.4. This allows us to calculate the normalized $\Delta U_{el,0}$ values, i.e. $\Delta U_{el,0}/(\mu d^3)$ for different measured θ' values (table 1) from the three-dimensional FE simulations as introduced in §3. Following a theoretical assumption proposed by Gent and Wang [39,40] that a small planar circular crack can be inflated into a spherical void of the same radius under a negligibly small initial pressure, we argue that p_0 is also negligible in an extremely soft and stretchable material exhibiting ductile failure response where $\tan\theta' \ll \tan\theta$. That is, the radial size of the undeformed crack is significantly smaller than that of the fully deformed cavity to accommodate the puncture tool. In this case, $\Delta U_{el,0}$ is minor compared with the total elastic energy ΔU_{el} to fully expand the cavity. In fact, this hypothesis is well supported by the relative magnitude of calculated $\Delta U_{el,0}/(\mu d^3)$ values as listed in table 1, which is on average one order of magnitude smaller than that of the normalized ΔU_{el} values (either from FE simulations or theoretical predictions) within our range of measurements and tested parameters. Further discussion on the applicable range and limitation of the above hypothesis is provided in §3.2.1.

To quantify the elastic deformation for the second step, we consider an equilibrium intermediate configuration during the expansion. At any arbitrary point having coordinates (r, y) (where r is the radial coordinate) on the cavity wall, we separate the axisymmetric inflating pressure/surface traction $p(r, y)$ into radial, $p_r(r, y)$, and vertical, $p_y(r, y)$, components (figure 3) to calculate their energy contributions, denoted as $\Delta U_{el,r}$ and $\Delta U_{el,y}$, respectively.

Consider a horizontal slice having an infinitesimal thickness, dy, at y (figure 3*c*). The effect of $p_r(r, y)$ within the slice can be approximated to the axisymmetric elastic expansion of a planar circular hole in an infinite material matrix from a radius $a(y)$ to $R(y)$ under *plane strain* conditions (figure 3*d*,*e*). Therefore, the radial energy contribution $\Delta U_{el,r}$ can be calculated by integrating the elastic work done per unit thickness over d [22]

$$\Delta U_{el,r} \approx \int_0^d \int_{a(y)}^{R(y)} p_r(r, y) 2\pi r\, dr\, dy. \tag{2.13}$$

Thus, finding $\Delta U_{el,r}$ is equivalent to determining $p_r(r, y)$ at equilibrium given the initial conditions $p_r = 0$ at $r = a(y)$. A detailed derivation for p_r is provided in the electronic supplementary material. Eventually, we may obtain p_r as a function of $a(y)$ and r in an incompressible neo-Hookean solid, normalized by the shear modulus, μ

$$\frac{p_r(r, y)}{\mu} = -\frac{1}{2}\left(\frac{r}{a(y)}\right)^{-2} + \ln\left(\frac{r}{a(y)}\right) + \frac{1}{2}. \tag{2.14}$$

Substituting equation (2.14) and the expressions for $a(y)$ and $R(y) = (d - y)\tan\theta$ into equation (2.13), we may obtain $\Delta U_{el,r}$ as

$$\Delta U_{el,r} = \frac{1}{3}\pi\mu(\tan^2\theta - \tan^2\theta')\ln\left(\frac{\tan\theta}{\tan\theta'}\right) d^3 \equiv k_r \mu d^3, \tag{2.15}$$

where the prefactor $k_r = \Delta U_{el,r}/(\mu d^3)$ is a dimensionless function of θ and θ'.

To calculate the vertical energy contribution, $\Delta U_{\mathrm{el},y}$, we relate $p_y(r, y)$ to $p_r(r, y)$ geometrically

$$p_y(r, y) = p_r(r, y)\frac{r}{d - y}. \tag{2.16}$$

Similar to the axisymmetric deformation described by equations (2.13), $\Delta U_{\mathrm{el},y}$ takes the following integral form:

$$\Delta U_{\mathrm{el},y} = \int_0^{R_0} 2\pi r \int_{y_0}^{y_1} p_y(r, y)\,\mathrm{d}y\,\mathrm{d}r, \tag{2.17}$$

where y_0 and y_1 denote y coordinates on the undeformed and fully deformed surfaces at r, respectively. Substituting equations (2.14) and (2.16) into equation (2.17), we can find a closed-form expression for $\Delta U_{\mathrm{el},y}$

$$\Delta U_{\mathrm{el},y} = k_y \mu d^3, \tag{2.18}$$

where

$$k_y = \pi\left[\frac{8}{27}\tan^3\theta' + \frac{1}{27}\tan^3\theta - \frac{1}{3}\tan^2\theta'\tan\theta + \frac{2}{9}\tan^3\theta\ln\left(\frac{\tan\theta}{\tan\theta'}\right)\right], \tag{2.19}$$

is a dimensionless prefactor.

Ultimately, ΔU_{el} can be obtained through the superposition

$$\begin{aligned}\Delta U_{\mathrm{el}} &= \Delta U_{\mathrm{el},0} + \Delta U_{\mathrm{el},r} + \Delta U_{\mathrm{el},y}\\ &= (k_0 + k_r + k_y)\mu d^3\\ &\approx (k_r + k_y)\mu d^3.\end{aligned} \tag{2.20}$$

We note that while normally a superposition principle of energy as a nonlinear function of displacement/strain components may introduce inaccuracy in a hyperelastic model, our calculations above are not subjected to such a systematic error, as we demonstrate through the comparison between theoretical predictions and FE simulation results in table 1 and figure 5. Because the contribution from $\Delta U_{\mathrm{el},0}$ is minor, and equations (2.13) and (2.17) are integrals having the same limits (which describe the boundaries of the undeformed and fully expanded cavities, respectively), the superposition of $\Delta U_{\mathrm{el},r}$ and $\Delta U_{\mathrm{el},y}$ is equivalently the summation of their integrands. Such a summation is a linear operation and is essentially the Cartesian components of the work done associated with an infinitesimal cavity growth, i.e. $\mathbf{F}\cdot\mathbf{ds} = F_x\,\mathrm{d}s_x + F_y\,\mathrm{d}s_y = (2\pi r \quad p_r\,\mathrm{d}y)\,\mathrm{d}x + (2\pi r\, p_y\,\mathrm{d}x)\,\mathrm{d}y$, where the integral of the infinitesimal work done, $\mathbf{F}\cdot\mathbf{ds}$, in the same integral space determines the stored elastic energy. A similar superposition principle adopted in the literature [22] further supports the above argument, which determines the elastic energy contribution to puncture associated with a cylindrical punch.

Equation (2.20) is beneficial in that it provides a closed-form, analytical approximation for ΔU_{el} in ductile soft materials. It implies a scaling relation

$$\Delta U_{\mathrm{el}} \sim d^3. \tag{2.21}$$

Apparently, ΔU_{el} scales with d similarly to W_f (equations (2.7) and (2.8)), but differently from W (equation (2.10)). This discrepancy in the scaling relations for the energy terms is anticipated—as d increases, because ΔU_{el} and W_f scale at a faster rate than W, at some point the energy expenditure to overcome the resistance from friction and deformation will become significantly larger than the energy required to fracture. Consequently, the total released fracture energy and the associated damage is limited for a finite external energy investment such as ΔE_k. Such speculation agrees with the results of previous experimental work on both arrows and viper fangs [5,17], which showed that the depth of puncture achieved was directly related to the kinetic energy available. After a certain depth is reached, overcoming friction/deformation requirements costs too much energy to sustain propagating puncture. Our theory supports this interpretation.

To summarize, we may combine the scaling relations of W_f, W and ΔU_{el} (i.e. equations (2.7), (2.10) and (2.20)) and re-write the total required energy for puncture, ΔE_k, (i.e. equation (2.4)) as a function of the depth of puncture, d, in a more general, non-dimensionalized form

$$\frac{\Delta E_k}{\mu\ell_c^3} = k_{\mathrm{frac}}\left(\frac{d}{\ell_c}\right)^2 + k_e\left(\frac{d}{\ell_c}\right)^3 + k_f\left(\frac{f}{\mu}\right)\left(\frac{d}{\ell_c}\right)^3, \tag{2.22}$$

where $\Delta E_k/(\mu\ell_c^3)$ and d/ℓ_c are the dimensionless energy of puncture and depth of puncture, respectively; the prefactor of each component is a dimensionless function of θ and θ', i.e. $k_{\mathrm{frac}} = \tan\theta'$, $k_e = k_0 + k_r + k_y$ and $k_f = (\pi/3)\tan\theta$ within our framework; and $\ell_c = \Gamma/\mu$ is a material characteristic length scale as we elaborate in §4.1. We argue based on the theory presented in electronic supplementary material, S1, that the general form of equation (2.22) always holds regardless of the choices of hyperelastic constitutive models, because their strain energy density functions take similar Taylor series forms [41]. While there is no simple-form analytical solution of d/ℓ_c from the cubic equation (equation (2.22)), a numerical solution is possible given specific puncture test conditions and material properties.

Overall, the above-derived scaling relations provide closed-form solutions to the governing energy balance equation for puncture (equation (2.4)). They allow us to quantitatively evaluate the relative magnitude of the required energy for puncture in terms of tool geometries and material properties. Particularly, the ratio between the fracture energy contribution and the total required puncture energy, $W/\Delta E_k$, contains key information about puncture tool versus material interactions. We discuss its further implications and potential applications as a performance metric for biological puncture efficiency in §4.1.

3. Visualization and verification

3.1. Visualization of puncture fracture

Understanding the morphology of the damage in a puncture system is important as it directly reflects the failure response of the tested material and provides a basis for quantifying the puncture performance. However, despite the abundance of previous studies on experimental and numerical puncture mechanics in soft polymers and biomaterials [5,16,17,19,21,23,26,28,36,42–44], only a handful of literature has explored the morphology of a post-puncture fracture surface following the removal of the tool; and the focus was mostly on the puncture failure caused by cylindrical or similar shaped tools. There is no guarantee that the conical-shaped puncture system ubiquitous in living organisms will exhibit similar failure responses. Therefore, it is necessary to visualize the damage produced by a sharp conical punch in comparison with the tool shape to verify the key morphological assumption underlying our

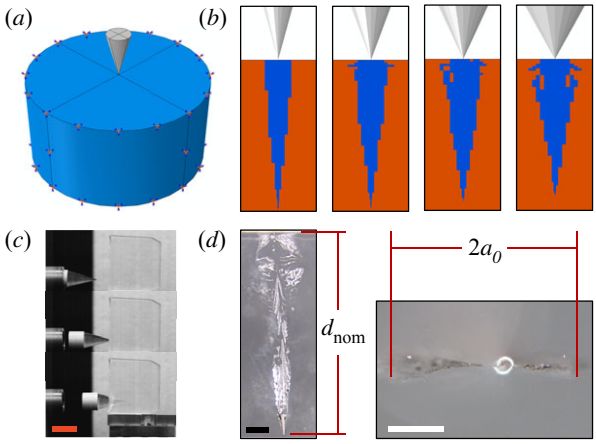

Figure 4. Visualization of puncture damage morphology. (*a*) Illustration of a three-dimensional FE assembly for puncture, which consists of a rigid conical surface representing a puncture tool ($2\theta = 30°$) and a cylindrical target material model. An 'encastre' boundary condition is applied on the bottom and side surfaces of the model. (*b*) Morphology of simulated puncture fracture surfaces (blue region) in the target material substrate (orange region) at a controlled depth of puncture. The subfigures from left to right correspond to puncture tool cusp angles, $2\theta = [30°,\ 40°,\ 50°,\ 60°]$, respectively. (*c*) High-speed images (10 000 fps) captured during a dynamic puncture test. The three-dimensional-printed projectile ($2\theta = 30°$) impacts and penetrates into the transparent target material sample until reaching the maximum depth of puncture (bottom frame). The interval between adjacent frames shown here is 15 frames. Orange scale bar: 2 cm (*d*). Microscopic images of the puncture fracture produced from a dynamic puncture test in (*c*). Left: side view of the undeformed fracture surface. Right: view showing the superficial crack on the impact surface. (A reflection of the LED ring light can be seen from the image.) The nominal depth of puncture (d_{nom}) and the superficial crack length ($2a_0$) are measured from the fracture surface as labelled in the corresponding subfigures. Scale bars: black: 1 mm; white: 500 µm.

energy theory of puncture in §2.2.3. In this section, we examine the morphology of the puncture fracture surface in neo-Hookean solids using both FE simulations and experimental methods.

The three-dimensional FE simulations for puncture implement a critical strain energy density (CSED) failure criterion to numerically simulate and visualize the finite damage associated with a conical puncture geometry penetrating an incompressible neo-Hookean material model (figure 4*a*) (see electronic supplementary material, S4.1 for technical details). The element deletion occurs to produce damage when the elemental strain energy density becomes comparable to the elastic modulus, which corresponds to a limiting tensile stretch, $\lambda \sim 3$, based on the neo-Hookean constitutive model [45,46]. It should be pointed out that due to the absence of defects and inhomogeneities in the implemented material model, the three-dimensional FE simulations produce nearly axisymmetric, conical-shaped fracture, and as such the released fracture energy is associated with the strain energy and volume of the 'damaged' elements. Despite the discrepancy in the apparent undeformed fracture morphology compared with our proposed model of a planar crack, we argue that such a numerical idealization does not systematically affect the evaluation of the damage size, or the magnitude of W or ΔU_{el} under the conditions we tested. Our assumed ductile failure response gives rise to an undeformed crack size smaller than the radial size of the puncture tool (i.e. condition (2.11)), which implies that the crack will become fully inflated into a conical cavity to accommodate the tool shape during fracture propagation, leaving a negligible gap at the tool–material interface. Consequently, for an infinitesimal radial crack growth da within a planar slice dy having a fully expanded circular cavity of radius $R(y)$ (i.e. the configuration illustrated by figure 3*e*), the stored strain energy within a ring-shaped volume described by $2\pi R(y)\,\mathrm{d}a\,\mathrm{d}y$ will be released because the material within this region can no longer bear the load in the circumferential direction. This released fracture energy is the same regardless of the number of crack fronts in the radial direction. (The proposed puncture model corresponds to two fronts while the finite-element analysis (FEA) corresponds to multiple crack fronts.) Ultimately, this leads to consistent estimations of the released strain energy, the undeformed crack size, and the stored elastic energy between the proposed model and the axisymmetric FE approach under the same prescribed puncture conditions and material properties (as verified in the following discussion). The difference between the two cases is in their definitions of the strain energy release rate which depend on their unique created fracture surface areas (e.g. the necessity to implement the mode-I toughness in the case of a planar crack). Further support can be found from a similar interpretation proposed for the irreversible growth of a spherical void [47].

Figure 4*b* shows the morphology of the simulated residual fracture surfaces in an undeformed configuration (blue region) as produced by four conical-shaped rigid punches having different cusp angles ($2\theta = [30°,\ 40°,\ 50°,\ 60°]$). As anticipated, the simulated fracture surfaces exhibit an approximately conical shape but have a significantly smaller taper angle than the corresponding shape necessary to accommodate the puncture cone. This behaviour agrees with the ductile failure response experimentally evident for a stretchable, neo-Hookean-like soft rubber [28].

In table 1, the nominal maximum puncture depth (d_{nom}, ESI) and the taper angle of the fracture surface ($2\theta'$) are measured from the undeformed FE configuration and listed for each applied cusp angle ($2\theta = [30°,\ 40°,\ 50°,\ 60°]$). The magnitude of d_{nom} is kept relatively constant via a controlled displacement (≈5 mm). The normalized work to fracture, $W/(\mu d^3)$, is computed from the three-dimensional FE simulations by integrating the released elemental energies across the material body. The result for each θ and θ' pair is compared with the corresponding theoretical scaling relation, normalized as

$$\frac{W}{\mu d^3} \sim \tan\theta' \left(\frac{\Gamma}{\mu}\right)\left(\frac{1}{d}\right). \tag{3.1}$$

It is assumed that the ratio between the material toughness and the shear modulus satisfies $\Gamma/\mu \sim 1$ mm, based on the previous mechanical characterization results [33] of our selected neo-Hookean-like model elastomer for the dynamic puncture testing introduced later (i.e. Solaris silicone elastomer, 1 : 1 weight mixing ratio, Smooth-on, Inc. (electronic supplementary material, S3) where the mode-I fracture energy $\Gamma \sim 130\,\mathrm{J\,m^{-2}}$ can be estimated from cutting tests to minimize additional dissipative effects; and the shear modulus $\mu \approx 0.13$ MPa was measured from uniaxial tension tests [33]). These values correspond to the stretchability of the

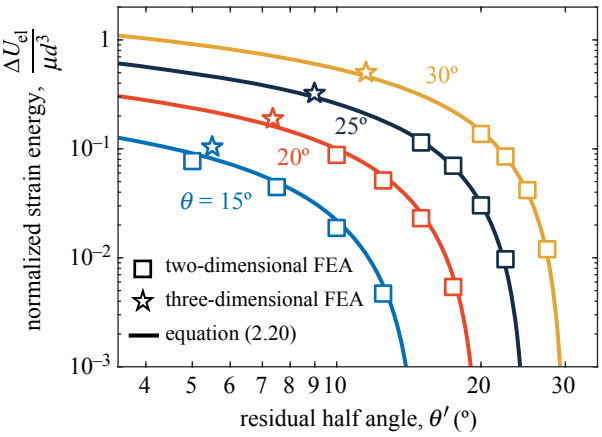

Figure 5. Comparison between FE results and theoretical predictions for the effects of puncture angles on the stored elastic strain energy. The approximate solution for the normalized total strain energy ($\Delta U_{el}/(\mu d^3) \approx k_r + k_y$, solid lines) is plotted for each of the four different half cusp angle values of the puncture tool ($\theta = 15°$, light blue; $\theta = 20°$, orange; $\theta = 25°$, dark blue; $\theta = 30°$, yellow). For each θ value, four different pre-notch half angle θ' values ($\theta' = \theta - [10°,\ 7.5°,\ 5°,\ 2.5°]$) are simulated using two-dimensional axisymmetric pre-notched FE tests (open squares). The strain energy results extracted from three-dimensional FE tests for puncture damage are also included (open pentagrams).

model elastomer (i.e. Solaris 1 : 1 mixing ratio, $\lambda \sim 3$) [33] that we implement for the CSED failure criterion in the FEA. We note from table 1 that the FE results and theoretical predictions for $W/(\mu d^3)$ find an order-of-magnitude agreement for all four cusp angles. The discrepancies in magnitude may be attributed to the estimation of Γ and the finite resolution of FEA. We also extract the normalized stored elastic energy $\Delta U_{el}/\mu d^3$ at the maximum puncture depth given the applied FE puncture conditions. The results are provided in table 1 and figure 5 and discussed in §3.2.1 in comparison to the strain energy verification results obtained from two-dimensional pre-notched FE tests and the corresponding theoretical predictions (equation (2.20)).

Experimental validation for puncture damage morphology is carried out using a customized compressed air cannon (Ballistic Loading and Structural Testing Lab, NC State University). The primary goals of the dynamic puncture testing are to: (i) validate the baseline assumption of a planar triangular crack in the undeformed configuration and (ii) verify our hypothesis in §2.2.3 that for a stretchable soft material exhibiting ductile failure response, the size of the undeformed fracture caused by puncture is significantly smaller than the size necessary to accommodate the puncture tool. During a puncture test, a three-dimensional printed conical projectile is launched towards a target material sample (Solaris silicone elastomer, 1 : 1 mixing ratio, electronic supplementary material, S3) at a controlled speed to produce puncture fracture (figure 4*c*). Further technical details of the dynamic puncture testing method are described in electronic supplementary material, S3. The speed at the onset of impact is determined from high speed photography (figure 4*c*) and post image processing to be approximately 9.8 m s^{-1}. Figure 4*d* shows microscopic images of a planar triangular fracture surface (side view) and its superficial seam crack (top view) created by a 30° puncture tool. The images were taken after the tool was removed from the material and the crack surface closed. The size of the superficial crack and the nominal maximum depth of puncture are estimated to be $2a_0 \approx 1.7$ mm, and $d_{nom} \approx 8.9$ mm, respectively, averaged between the measurements from both microscopic image processing and manual probing. These dimensions give an estimation for the half taper angle of the residual fracture surface: $\theta' \approx 5.6°$. This result coincides with the θ' value ($\theta' \approx 5.5°$) measured from the corresponding three-dimensional FE simulation (i.e. $2\theta = 30°$), which implements the failure properties of the tested Solaris silicone elastomer. Particularly, we note that the estimated taper angle is significantly smaller than the cusp angle of the puncture cone, which well agrees with our proposed ductile puncture failure behaviour (§2.2.3). This fracture response is expected and can be attributed to the neo-Hookean constitutive behaviours of the selected target material, which has been demonstrated through mechanical characterization up to a strain of approximately 100% [33].

Finally, future puncture experiments are necessary to include systematic characterization of the puncture energies to verify the theoretical predictions as well as the FEA results for the relationship between energy, or force and depth of puncture given prescribed material properties and testing conditions. While quasi-static puncture characterization (e.g. [1,4,8,48]) and puncture experiments on cylindrical and similar shaped tools (e.g. [3,19,22,25,28,36]) have been performed previously, there still lacks sufficient data from dynamic puncture testing to verify our puncture model; complications may arise from various aspects including but not limited to:

- It is difficult to directly measure the force–displacement response during a dynamic puncture test without modifying the existing test system and redesigning the projectile structure.
- Experimental characterization of the individual puncture energy components (ΔU_{el}, W and W_f) requires decoupling from the total loss of kinetic energy/external work done, ΔE_k. This is not possible without a knowledge of the force–displacement response or the full stress/strain field near the puncture damage.
- The interfacial frictional properties are largely unknown under biological, dynamic puncture environments (§4.2).

Addressing these complications will facilitate the development of novel mechanical characterization methods incorporated into the existing experimental puncture system.

3.2. Finite-element verification for stored strain energy

This section presents the simulated results for ΔU_{el} obtained from two-dimensional axisymmetric pre-notched FE models having an incompressible neo-Hookean constitutive response (see electronic supplementary material, S4.2 for technical details). Both the effect of puncture angles (θ and θ') on ΔU_{el} and the scaling relation for ΔU_{el} are quantitatively investigated. The numerical results are compared with corresponding theoretical predictions across a wide range of test conditions to verify the proposed mathematical model in §2.2.4.

3.2.1. Puncture angle effects

Figure 5 shows the simulated ΔU_{el} values (normalized by μ and d) (open squares) for different selected θ and θ' puncture angle combinations obtained from two-dimensional axisymmetric pre-notched FEA (electronic supplementary

material, S4.2). The FE results are directly compared with non-dimensionalized theoretical predictions for total elastic contributions, i.e. $\Delta U_{el}/(\mu d^3) \approx k_r + k_y$ (solid lines, equation (2.20), note the contribution from $\Delta U_{el,0}$ is neglected to directly compare with the two-dimensional axisymmetric simulations). The close agreement between the simulations and the theory in magnitude across wide angle ranges (figure 5; electronic supplementary material, S4.2) verifies the dimensionless prefactor, $k_r + k_y$, which depends on θ and θ' (equations (2.15) and (2.19)). This quantitative match also suggests that the elastic contribution from indentation (i.e. that associated with d_e (figure 2)) is negligible. As figure 5 indicates, ΔU_{el} decreases rapidly with increasing θ' or decreasing θ. Such observation is consistent with the anticipated puncture response for a sharp, slender tool versus a wide tool (§2.2.4).

However, it should be noted that as θ' approaches θ, the assumption of ductile failure response becomes no longer accurate. In this case, the axisymmetric elastic energy contribution (i.e. $\Delta U_{el,r} + \Delta U_{el,y}$) vanishes and the contribution from $\Delta U_{el,0}$ needs to be taken into account to evaluate the elastic strain energy associated with a planar triangular undeformed crack. In electronic supplementary material, S4.5, we calculate and plot the theoretical relative magnitude of $\Delta U_{el,0}$, i.e. $\Delta U_{el,0}/\Delta U_{el} = k_0/(k_0 + k_r + k_y)$ as a function of the ratio, $\tan\theta/\tan\theta'$ for four different θ values (coloured solid lines, $2\theta = [30°, 40°, 50°, 60°]$). It is found that the contribution of $\Delta U_{el,0}$ becomes significant (i.e. $\Delta U_{el,0}/\Delta U_{el} \gtrsim 0.1$) when on average $\tan\theta/\tan\theta' < 2.7$. For comparison, the average ratio calculated from our three-dimensional FE measurements (table 1) is $\tan\theta/\tan\theta' \approx 2.85 \pm 0.07$. Moreover, the observation from electronic supplementary material, figure S4 that all theoretical curves collapse to nearly a single master curve and the similar values of the ratio $\tan\theta/\tan\theta'$ from the three-dimensional FEA at different θ values have two interesting implications: (i) the relative magnitude of $\Delta U_{el,0}$ is governed by $\tan\theta/\tan\theta'$, i.e. the radial size of the fully deformed crack relative to that of the undeformed crack; and (ii) $\tan\theta/\tan\theta'$ appears to be a material constant independent of puncture tool geometry (θ). We speculate that it is related to the stretchability of the target material. Overall, these findings provide evidence for and quantitatively define the physical constraint of our hypothesis in §2.2.4—the energy contribution of $\Delta U_{el,0}$ is minor only in highly stretchable and tough soft materials exhibiting a small undeformed crack size.

In table 1 and figure 5, we also include the $\Delta U_{el}/(\mu d^3)$ values corresponding to the four different cusp angles ($2\theta = [30°, 40°, 50°, 60°]$) and their measured θ' values (table 1), computed from three-dimensional FE simulations for puncture damage (§3.1). The combined results from both two-dimensional axisymmetric and three-dimensional FE simulations together cover a large range (over a decade) of possible θ' values for each selected θ value ($0 < \theta' < \theta$). However, we emphasize that in soft, highly deformable elastomers exhibiting ductile failure behaviours (e.g. Solaris 1 : 1 mixing ratio) and our three-dimensional FEA using the neo-Hookean material model, the measured θ' values are found to be at the lower end of the spectrum (e.g. figure 5) presumably due to the high stretchability of the materials. A close match between the FE results and the theoretical predictions for $\Delta U_{el}/(\mu d^3)$ (from either the full form (table 1) or the approximation (figure 5)) is evident. This in combination with the discussion above verifies: (i) the strain energy theory in §2.2.4 and the minor contribution from $\Delta U_{el,0}$ for our selected model materials and test conditions; and (ii) the trend that ΔU_{el} increases with increasing cusp angle θ. Particularly, it seems that the change of $2\theta'$ as 2θ increases has a minor effect on the trend of ΔU_{el} in a neo-Hookean solid, judging by the relative magnitude in table 1.

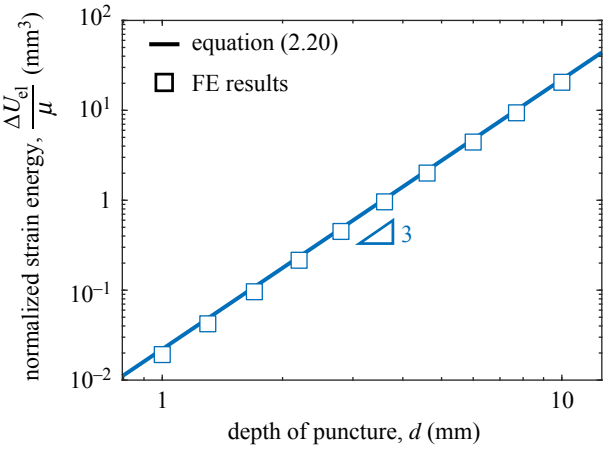

Figure 6. Verification of the scaling relation between ΔU_{el} and d. The selected half angle values are $\theta = 15°$ for the puncture tool and $\theta' = 10°$ for the pre-notch representing the fracture surface, respectively. The theory for modulus normalized strain energy (equation (2.20), solid line) predicts that $\Delta U_{el}/\mu \sim d^3$. The simulated $\Delta U_{el}/\mu$ values (open squares) collapse on the theoretical master curve on a log-log scale.

3.2.2. Scaling relation verification for stored strain energy

Figure 6 is a log-log plot comparing the scaling relations between $\Delta U_{el}/(\mu)$ and d as predicted by equation (2.20) (solid line) and numerically simulated through the two-dimensional axisymmetric FE method ($\theta = 15°$ and $\theta' = 10°$, electronic supplementary material, S4.2) (open squares). We emphasize that no data fitting is implemented in figure 6. Regardless, the FE data points collapse on the theoretical scaling curve corresponding to $\Delta U_{el}/(\mu) \approx (k_r + k_y)\, d^3$. The satisfactory agreement between the prediction and the FE results in both magnitude and slope quantitatively supports the proposed scaling relation in §2.2.4 (i.e. $\Delta U_{el} \sim d^3$, equation (2.21)).

Overall, the FE and experimental visualization provides strong evidence for the proposed condition (2.11) that the puncture damage has a size significantly smaller than that necessary to accommodate the tool in a highly deformable, neo-Hookean material exhibiting ductile failure response. Moreover, the dynamic puncture experiments verify our baseline morphological assumption of a planar triangular crack in the undeformed configuration. The close match between the numerical estimations and the theoretical predictions in table 1 and figure 5 quantitatively supports our puncture energetic model (§2). The visualization and verification presented here lay the foundation for implementing the puncture energy theory to help in characterizing biological puncture systems. However, it is important to recognize that biological puncture systems associated with brittle failure response, such as egg shell puncture [49] and chitinous beetle shell puncture [50], are not uncommon. Brittle crack extension and branching may markedly change the damage morphology [28,36,42] and, consequently, increase the damage size and the contribution to the released fracture energy relative to the stored strain energy—an avenue for future research.

4. Discussion

The above quantitative verification supports the puncture energy theory as a theoretical framework to contextualize puncture systems in living organisms. As demonstrated in §2, both a close-form expression and the corresponding scaling relation are provided for each energy component associated with puncture (W_f, W and ΔU_{el}). These exact solutions enable a practical, quantitative approach for estimating the magnitudes of energy contributions in biological puncture systems. Particularly, the verified energy components for damage creation and elastic deformation (i.e. W and ΔU_{el}) consist of quantities that are experimentally measurable through mechanical characterization of biomaterials including puncture failure tests (θ, θ' and d), uniaxial tensile tests (μ), and tearing fracture tests (Γ) [31,33,51]. In the following sections, we use this model as a springboard for exploring and discussing potential biomechanical applications and biological implications including puncture performance in terms of energy efficiency (§4.1), the complexity of puncture systems (§4.2) and overall scaling in puncture systems (§4.3).

4.1. Energy ratio as a puncture performance metric

Although puncture mechanisms have been identified in numerous biological systems [12], it is challenging to identify a general performance metric that can quantify puncture efficiency across biological systems for comparative studies. An effective performance metric should both serve as a mathematical tool to evaluate the relative performance of puncture systems [4] and provide a quantitative trait for use in ecomechanical models [52], studies of evolutionary convergence [10,12] and morphological diversity [1,53]. However, the interplay between puncture tool morphology, biomaterial properties and fracture mechanics significantly complicates the characterization of puncture biomechanics.

Previous performance metrics used in studies on biological puncture have included functional 'sharpness' [1,4,9,12,18,54], puncture force [1,3,8,9,18,19,48] or energy associated with puncture [2–4,7,8,12,21,28,48,55] to characterize the effectiveness of biological puncture systems. These approaches often focus on only one aspect of the puncture system. For example, many studies define 'sharpness' index [4,18,34] or an equivalent quantity [1] that accurately describes the geometric factors (e.g. radius of curvature and tip included angle) controlling the shape of a puncture/cutting tool. However, the relationship between these morphological measures and actual puncture performance are not clear [1,4,18,19,34,56]. Further complications arise when material response is introduced. There is no guarantee that a 'sharp' puncture tool for one biological material will retain its functional 'sharpness' for a different material, as puncture response changes with material properties [28,57]. Therefore, functional 'sharpness' can only be regarded as a relative metric restricted to a specific puncture environment.

Other performance metrics extract force/energy measurements directly from puncture tests [1–5,8,11,17,48,49,58]. These measures do not contain explicit information about either puncture tool shapes or material properties. Therefore, they are only meaningful for single-variable, controlled comparative studies. Theoretically, it is possible to find two puncture systems with similar force responses but completely different energetic compositions (e.g. W versus ΔU_{el}) by adjusting materials or morphologies (e.g. [3]), making performance evaluation difficult.

To address these complications and limitations of conventional metrics, we propose a quantity based on our energy theory—the ratio between the fracture work and the total required energy for puncture at a puncture depth d, i.e. $W/\Delta E_k$—as a performance metric for puncture efficiency. It takes a general form, based on equation (2.22),

$$\frac{W}{\Delta E_k} = \left\{1 + \left[\frac{k_e}{k_{frac}} + \frac{k_f}{k_{frac}}\left(\frac{f}{\mu}\right)\right]\left(\frac{d}{\ell_c}\right)\right\}^{-1}. \tag{4.1}$$

The magnitude of the ratio $W/\Delta E_k$ ranges from 0 to 1. A larger magnitude indicates that a higher proportion of energy is contributed to fracture propagation relative to the total energy investment. By definition, such a puncture system corresponds to higher energy efficiency and is more beneficial for the puncturing organism. An ideal puncture system should require a minimal amount of deformation and dissipation (including the work to overcome friction) to sustain the failure propagation. As demonstrated by equation (4.1), the ratio $W/\Delta E_k$ quantitatively relates several important factors that influence puncture performance: (i) puncture tool geometries (θ); (ii) material failure response (Γ and θ'); (iii) material elastic properties (μ); (iv) frictional effect (f); and (v) depth of puncture (d). Based on equation (4.1), a higher efficiency coefficient can be achieved with any combination of the following:

— a relatively large characteristic length scale, ℓ_c;
— a relatively small depth of puncture, d;
— a relatively small ratio f/μ.

In table 1, we show the efficiency coefficient $W/\Delta E_k$ for four different cusp angles ($2\theta = [30°, 40°, 50°, 60°]$) obtained from three-dimensional puncture simulations (electronic supplementary material, S4.1), in comparison with the corresponding theoretical predictions from equation (4.1). In FEA, we assume a negligible frictional contribution and $f/\mu \approx 0$ to explore the effect of variations in puncture tool geometries on the upper limit of the efficiency coefficient given the same material properties and depth of puncture d. Within our range of measurements, both the simulation results and the theoretical predictions indicate decreasing puncture efficiency as 2θ increases. This trend can be identified by evaluating the governing prefactor in equation (4.1) when $f = 0$ (i.e. $k_e/k_{frac} = (k_0 + k_r + k_y)/k_{frac}$) as a function of θ and θ' (electronic supplementary material, figure S5). For cusp angles ranging from $2\theta = 30°$ to $2\theta = 60°$ at similar d_{nom}, the increment in ΔU_{el} outpaces in relative magnitude the increment of W due to the enlarged $2\theta'$ value. This behaviour may stem from both the failure response of a neo-Hookean solid (which controls the magnitude of $2\theta'$) and the different scaling orders between ΔU_{el} and W. The importance of 2θ to tool shape has been demonstrated experimentally in numerous biological systems including mammal teeth [1,50], arthropod elements [3] and snake fangs [4]. While those studies illustrated experimental effects, we can now place them into the context of this framework and our metric.

To better understand the effect of material response on puncture efficiency, it is necessary to discuss the fracture-relevant characteristic length scale, $\ell_c \sim \Gamma/\mu$. The ratio

between fracture toughness and stiffness has been widely used in experimental and theoretical fracture mechanics. Broadly, it defines a physical length scale which, when compared with the failure or sample size (e.g. d), predicts critical conditions necessary for failure and failure transitions. Examples of this include the modulus normalized pressure of puncture initiation for soft rubbers and skins [28]; the fragmentation criterion for food–tooth interactions [59]; or the transition to a nonlinear, fracture-relevant regime as the crack tip is approached during tearing failure ($\ell_c \sim \ell_e$, electronic supplementary material) [32,33]. It is anticipated from equation (4.1) that when $d \gg \ell_c$, the puncture efficiency coefficient $W/\Delta E_k \to 0$, and therefore, elastic contribution (ΔU_{el}) and frictional dissipation (W_f) dominate over fracture contribution (W). Consequently, the propagation of puncture fracture is limited because of the extremely large resistance. We note this is a limit relatively easy to achieve for dynamic puncture in neo-Hookean-like soft polymers where $\ell_c \sim 0.1$–1 mm is typical and ductile failure response prevails [32,33].

In summary, the integration of the effects of puncture tool geometries, material elasticity, frictional dissipation and failure response in the puncture efficiency coefficient ($W/\Delta E_k$) offers a quantitative approach to multi-variable, comparative analysis of puncture performance. However, it should be noted that in complex soft polymers and biomaterials, the determination of fracture energy is highly material and failure condition dependent [32]. According to equation (2.9), only when additional bulk dissipative effects (i.e. that relate to Γ_d) such as viscoelasticity and the Mullins effect [32] are minimized can the measured strain energy release rate (i.e. G_c) be a reasonable estimation for the material toughness Γ. Moreover, the strength of the puncture tool, e.g. the resistance to fracture, buckling [15] and wear and attrition [54], may also be a significant factor to affect the efficiency and the limitation of puncture—an interesting future direction to explore.

4.2. Effect of friction on puncture biomechanics

In the above verification and discussion, we neglect the effect of frictional work on puncture energetics. One reason is that frictional work, W_f, associated with conical puncture is relatively independent compared with the other two components. It is determined solely by puncture tool morphology (e.g. θ) and the depth of puncture (d), independent of either material stiffness or fracture response based on equation (2.7). It is reasonable to speculate that in a scenario where a slender tool punctures a stiff/tough material with relatively high Γ and μ values, W_f will be minor compared with W and ΔU_{el}. Therefore, our previous conclusions hold regardless of W_f. Even where W_f is not negligible in magnitude, it is unlikely to alter the damage morphology or the trend of the efficiency coefficient $W/\Delta E_k$ (equation (4.1)) given predetermined puncture tool morphology, material properties and depth of puncture. However, as d increases, eventually W_f will exceed W as W_f scales with d by an order higher than W ($W_f \sim d^3$ versus $W \sim d^2$). This suggests that friction energy may be significant for biological puncture systems requiring large depth of puncture, such as feeding [60] or burrowing to deposit eggs [14], and may become less important for systems designed for, e.g. gripping [6] or self-defence [7].

The above argument necessitates an estimation of frictional work as a substantial part of energy dissipation in the case of deep biological puncture (relative to the puncture tool length). Complications arise for quantification of W_f in determination of the friction force per unit area, f, as an interfacial parameter (equation (2.7)). Alternatively, f can be expressed as $f = \eta p_{app}$ [15,26], where p_{app} is the average interfacial pressure between the puncture tool and the material, and η is the friction coefficient. It can be shown from the general form of the puncture energy presented by equation (2.22) that regardless of the constitutive model implemented, p_{app} can be generally expressed as, normalized by the shear modulus, μ,

$$p_{app} = \frac{\partial \Delta E_k}{\partial d} \cdot \frac{1}{\mu A_{proj}} = A + B\frac{\ell_c}{d}, \tag{4.2}$$

where $A_{proj} = \pi \tan^2\theta d^2$ is the projection area of the puncture cone at d; and A and B are dimensionless functions of θ and material failure properties. Therefore, for a large d value where $d \gg \ell_c$, $p_{app} \approx A$ is approximately a constant and as such f is approximately a constant for the same puncture tool and target material. Nevertheless, in biological puncture systems, internal mechanical processes such as muscular contractions [15] and poroelasticity driven by tissue fluid transportation [61] can increase the magnitude of p_{app} by an order of 10 kPa [15] or higher depending on the local deformation. Further uncertainty emerges when estimating the friction coefficient η. Experimental work has shown that η is highly sensitive to surface roughness, and such dependence is governed by a 'true' contact area at a microscale [62]. In biological tissues, contact mechanics can be even more complicated when the effects of surface adhesion [26,63], hierarchical structures [63], ornamentation [7,9,11,48] or lubrication [57] are introduced. Organic puncture tools such as mosquito proboscis [11], stingray barbs [9], parasitic wasp ovipositor [14], porcupine quill [48] and cactus spine [7] often exhibit morphological ornamentations or microstructured serrations. Experimental work has shown that these microstructures may reduce friction associated with puncture by minimizing contact area [7,11,48]. Characterization of the friction contribution in biological puncture systems requires examining the specific contact conditions and material properties. Our theoretical framework allows extra variables to be included in future applications with emphasis on puncture tool morphology and contact area to better understand the effect of friction on biological functions and puncture efficiency.

4.3. On the scaling of biological puncture

A growing body of literature exists investigating scaling in biological puncture systems [3,15,18,53,54,64–66]. Puncture tools used by organisms across a wide range of taxa often show a high degree of morphological convergence despite their drastic differences in sizes [12,15]. A fundamental yet challenging question remains in understanding the mechanism underlying this convergence: What is a proper length scale to establish general scaling relationships with characteristics of puncture (such as tool sharpness and energetics)? Many previous studies [3,53,54,66] explored the scaling between puncture tool sharpness and body length/mass. However, there is no consensus for generalization or a universal governing scaling law across different taxa. While this

complication can partially arise from the effect of wear and attrition [54] on tool morphology, a more core reason may be that whole body scale is not directly linked to, and thus does not reflect, the interactions between puncture tool and target material.

Canine tooth morphology in mammals, for example, exhibits a strong correlation with diet [53]. Thus, it is not surprising that the canine teeth of a clouded leopard (*Neofelis nebulosa*) and an ocelot (*Leopardus pardalis*) exhibit similar 'sharpness' [1] indices despite significant difference in body length/mass. In an extreme case, small insectivorous microchiropterans have some of the sharpest canine teeth among mammals [18,67]. However, the correspondence between their tooth sharpness and body mass fails to fit the scaling trend for medium–large mammals [54]. In this case, the sharpness is probably a result of a combination of tooth development [54], tooth strength and dietary requirements [67].

On a broader scale, there is difficulty inherent in comparing scales because the tool itself may be at very different scales in relation to the organism using them. How does one compare the canine tooth of a tiger, which is probably no more than 1% of its overall body length, with the ovipositor of a wasp, which can reach up to 50% of its body length? In each case, different muscles actuate the tool, which probably have their own scaling relationships with both body size and tool size.

Ultimately, what determines the performance of puncture is the failure response (e.g. energy required for puncture) governed by both puncture tool morphology and target material properties. Therefore, a fundamental scaling relationship should theoretically exist between a proper puncture performance metric and a length scale associated with puncture failure. In our puncture energy theory (§2), such scaling can be established between the depth of puncture d and each of the energy components included in our model (W, W_f and ΔU_{el}), including a performance coefficient ($W/\Delta E_k$, equation (4.1)). These correspondences can provide a biomechanical baseline for general scaling relationships of puncture in living organisms. Future applications may include investigation of the cause of the morphological convergence in puncture tools and exploration of the scaling with muscle size—muscles and tendons physically supporting the puncture tool act functionally like a spring [6,68]; thus, their length scales may be related to the force or energy necessary for puncture failure via a generalized Hooke's Law [69]. Broadly, our model enables expansion with scaling laws in biological puncture systems through generalization of the effects of puncture tool morphology and material properties on the energetics.

5. Conclusion

We have presented a baseline theoretical framework for puncture energetics that offers a timely analytical approach to biomechanically contextualize and systematically characterize biological puncture systems across a wide range of scales and taxa. While open questions remain regarding assumptions made in this study, the model presented creates multiple avenues for future inquiry. Examples of such future work could involve exploring the effects of variation in biomaterial properties such as brittleness, toughness and deformability in our hyperelastic material model; and how they affect puncture failure response. For instance, how does puncture efficiency vary across materials such as skins [28], muscle and fat [57]. While the neo-Hookean constitutive model we used in this work is beneficial for quantification for its simplicity, it does not well represent some of the large-strain nonlinear behaviours of complex biological composites and tissues. Fortunately, our current general model has mathematically enabled the future incorporation of more complex, nonlinear material response such as strain-stiffening via a more general constitutive model (see electronic supplementary material, S1). Other major factors to be explored in future work include dynamic effects arising from rate-dependent material responses including viscoelasticity and strain-rate hardening [70] at higher impact speeds; and the effect of large puncture tool tip radii exceeding the minimum length scale for failure (i.e. $r_{\mathrm{tip}} > \ell_f$). The former may introduce significant bulk dissipation to total fracture energy (equation (2.9), §2.2.3), while the latter may break the small-scale-yield-like condition and significantly increase the required elastic contribution for puncture due to the enlarged deformation (ℓ_e) near the tip. A FE-assisted approach similar to those implemented for cutting [33] may be necessary to quantify the elasticity associated with finite tip radii.

We hope that this analytical model can help to focus future work on biological puncture systems by offering both specific parameters for measurement/analysis as well as a general framework for comparing highly disparate systems on a level playing field.

Data accessibility. The script used for simulations is provided as electronic supplementary material. The data are provided in electronic supplementary material [71].

Authors' contributions. B.Z.: conceptualization, data curation, formal analysis, investigation, methodology, software, validation, visualization, writing—original draft, writing—review and editing; P.S.L.A.: conceptualization, funding acquisition, project administration, resources, supervision, writing—original draft, writing—review and editing.

All authors gave final approval for publication and agreed to be held accountable for the work performed therein.

Conflict of interest declaration. We declare we have no competing interests.

Funding. This work was supported by the National Science Foundation (grant no. NSF IOS 19-42906 CAR to P.S.L.A.).

Acknowledgements. The authors would like to thank Dr Stephanie Crofts for insightful comments as well as Lei Hu for help with mathematical review. We also extend our gratitude to the two anonymous reviewers for their constructive feedback that greatly improved this manuscript.

References

1. Freeman P, Lemen C. 2007 The trade-off between tooth strength and tooth penetration: predicting optimal shape of canine teeth. *J. Zool.* **273**, 273–280. (doi:10.1111/j.1469-7998.2007.00325.x)
2. Whitenack L, Motta P. 2010 Performance of shark teeth during puncture and draw: implications for the mechanics of cutting. *Biol. J. Linnean Soc.* **100**, 271–286. (doi:10.1111/j.1095-8312.2010.01421.x)
3. Schofield R, Choi S, Coon J, Goggans M, Kreisman T, Silver D, Nesson M. 2016 Is fracture a bigger problem for smaller animals? Force and fracture scaling for a simple model of cutting, puncture and

crushing. *Interface Focus* **6**, 20160002. (doi:10.1098/rsfs.2016.0002)

4. Crofts S, Lai Y, Hu Y, Anderson P. 2019 How do morphological sharpness measures relate to puncture performance in viperid snake fangs? *Biol. Lett.* **15**, 20180905. (doi:10.1098/rsbl.2018.0905)
5. Anderson P, Crofts S, Kim J, Chamorro L. 2019 Taking a stab at quantifying the energetics of biological puncture. *Integr. Comp. Biol.* **59**, 1586–1596. (doi:10.1093/icb/icz078)
6. DeVries M, Murphy E, Patek S. 2012 Strike mechanics of an ambush predator: the spearing mantis shrimp. *J. Exp. Biol.* **215**, 4374–4384. (doi:10.1242/jeb.075317)
7. Crofts S, Anderson P. 2018 The influence of cactus spine surface structure on puncture performance and anchoring ability is tuned for ecology. *Proc. R. Soc. B* **285**, 20182280. (doi:10.1098/rspb.2018.2280)
8. Galloway K, Porter M. 2021 Predator–prey interactions examined using lionfish spine puncture performance. *Integr. Org. Biol.* **3**, obaa049. (doi:10.1093/iob/obaa049)
9. Shea-Vantine C, Galloway K, Ingle D, Porter M, Kajiura S. 2021 Caudal spine morphology and puncture performance of two coastal stingrays. *Integr. Comp. Biol.* **61**, 749–758. (doi:10.1093/icb/icab077)
10. Bar-On B. 2019 On the form and bio-mechanics of venom-injection elements. *Acta Biomater.* **85**, 263–271. (doi:10.1016/j.actbio.2018.12.030)
11. Li A, Putra K, Chen L, Montgomery J, Shih A. 2020 Mosquito proboscis-inspired needle insertion to reduce tissue deformation and organ displacement. *Sci. Rep.* **10**, 1–14. (doi:10.1038/s41598-020-68596-w)
12. Anderson P. 2018 Making a point: shared mechanics underlying the diversity of biological puncture. *J. Exp. Biol.* **221**, jeb187294. (doi:10.1242/jeb.187294)
13. Britt E, Clark A, Bennett A. 2009 Dental morphologies in gartersnakes (*Thamnophis*) and their connection to dietary preferences. *J. Herpetol.* **43**, 252–259. (doi:10.1670/08-109R1.1)
14. Cerkvenik U, Straat B, Gussekloo S, Leeuwen J. 2017 Mechanisms of ovipositor insertion and steering of a parasitic wasp. *Proc. Natl Acad. Sci. USA* **114**, E7822–E7831. (doi:10.1073/pnas.1706162114)
15. Jensen K, Knoblauch J, Christensen A, Haaning K, Park K. 2020 Universal elastic mechanism for stinger design. *Nat. Phys.* **16**, 1074–1078. (doi:10.1038/s41567-020-0930-9)
16. Fakhouri S, Hutchens S, Crosby A. 2015 Puncture mechanics of soft solids. *Soft Matter* **11**, 4723–4730. (doi:10.1039/C5SM00230C)
17. Anderson P, LaCosse J, Pankow M. 2016 Point of impact: the effect of size and speed on puncture mechanics. *Interface Focus* **6**, 20150111. (doi:10.1098/rsfs.2015.0111)
18. Freeman P, Weins W. 1997 Puncturing ability of bat canine teeth: the tip. *Spec. Publ. Mus. Southwest. Biol.* **3**, 226–231.
19. Nguyen C, Vu-Khanh T, Dolez P, Lara J. 2009 Puncture of elastomer membranes by medical needles. Part I: mechanisms. *Int. J. Fract.* **155**, 75–81. (doi:10.1007/s10704-009-9326-7)
20. Fregonese S, Bacca M. 2021 Piercing soft solids: a mechanical theory for needle insertion. *J. Mech. Phys. Solids* **154**, 104497. (doi:10.1016/j.jmps.2021.104497)
21. Stevenson A, Malek K. 1994 On the puncture mechanics of rubber. *Rubber Chem. Technol.* **67**, 743–760. (doi:10.5254/1.3538707)
22. Shergold O, Fleck N. 2004 Mechanisms of deep penetration of soft solids, with application to the injection and wounding of skin. *Proc. R. Soc. Lond. A* **460**, 3037–3058. (doi:10.1098/rspa.2004.1315)
23. Nguyen C, Vu-Khanh T, Dolez P, Lara J. 2009 Puncture of elastomer membranes by medical needles. Part II: mechanics. *Int. J. Fract.* **155**, 83–91. (doi:10.1007/s10704-009-9325-8)
24. Fakhouri S. 2015 Cavitation and puncture for mechanical measurement of soft solids. PhD thesis, University of Massachusetts Amherst, Amherst, MA.
25. Rattan S, Crosby A. 2019 Effect of polymer volume fraction on fracture initiation in soft gels at small length scales. *ACS Macro Lett.* **8**, 492–498. (doi:10.1021/acsmacrolett.9b00086)
26. Fregonese S, Bacca M. 2022 How friction and adhesion affect the mechanics of deep penetration in soft solids. *Soft Matter* **18**, 6882–6887. (doi:10.1039/d2sm00638c)
27. Vogel S. 2013 *Comparative biomechanics: life's physical world*. Princeton, NJ: Princeton University Press.
28. Shergold O, Fleck N. 2005 Experimental investigation into the deep penetration of soft solids by sharp and blunt punches, with application to the piercing of skin. *J. Biomech. Eng.* **127**, 838–848. (doi:10.1115/1.1992528)
29. Long R, Hui C. 2016 Fracture toughness of hydrogels: measurement and interpretation. *Soft Matter* **12**, 8069–8086. (doi:10.1039/C6SM01694D)
30. Griffith A. 1921 VI. The phenomena of rupture and flow in solids. *Phil. Trans. R. Soc. Lond. A* **221**, 163–198. (doi:10.1098/rsta.1921.0006)
31. Creton C, Ciccotti M. 2016 Fracture and adhesion of soft materials: a review. *Rep. Prog. Phys.* **79**, 046601. (doi:10.1088/0034-4885/79/4/046601)
32. Long R, Hui C, Gong J, Bouchbinder E. 2021 The fracture of highly deformable soft materials: a tale of two length scales. *Annu. Rev. Condens. Matter Phys.* **12**, 71–94. (doi:10.1146/annurev-conmatphys-042020-023937)
33. Zhang B, Hutchens S. 2021 On the relationship between cutting and tearing in soft elastic solids. *Soft Matter* **17**, 6728–6741. (doi:10.1039/D1SM00527H)
34. McCarthy C, Annaidh A, Gilchrist M. 2010 On the sharpness of straight edge blades in cutting soft solids: part II—analysis of blade geometry. *Eng. Fract. Mech.* **77**, 437–451. (doi:10.1016/j.engfracmech.2009.10.003)
35. Milner M, Hutchens S. 2021 Dynamic fracture of expanding cavities in nonlinear soft solids. *J. Appl. Mech.* **88**. (doi:10.1115/1.4051431)
36. Lin W, Otim K, Lenhart J, Cole P, Shull K. 2009 Indentation fracture of silicone gels. *J. Mater. Res.* **24**, 957–965. (doi:10.1557/jmr.2009.0128)
37. Nüchter T, Benoit M, Engel U, Özbek S, Holstein T. 2006 Nanosecond-scale kinetics of nematocyst discharge. *Curr. Biol.* **16**, R316–R318. (doi:10.1016/j.cub.2006.03.089)
38. Patek S, Baio J, Fisher B, Suarez A. 2006 Multifunctionality and mechanical origins: ballistic jaw propulsion in trap-jaw ants. *Proc. Natl Acad. Sci. USA* **103**, 12 787–12 792. (doi:10.1073/pnas.0604290103)
39. Gent A, Wang C. 1991 Fracture mechanics and cavitation in rubber-like solids. *J. Mater. Sci.* **26**, 3392–3395. (doi:10.1007/BF01124691)
40. Lin Y, Hui C. 2004 Cavity growth from crack-like defects in soft materials. *Int. J. Fract.* **126**, 205–221. (doi:10.1023/B:FRAC.0000026510.60747.3a)
41. Anssari-Benam A, Bucchi A. 2021 A generalised neo-Hookean strain energy function for application to the finite deformation of elastomers. *Int. J. Non-Linear Mech.* **128**, 103626. (doi:10.1016/j.ijnonlinmec.2020.103626)
42. Oldfield M, Dini D, Giordano G, Rodriguez y Baena F. 2013 Detailed finite element modelling of deep needle insertions into a soft tissue phantom using a cohesive approach. *Comput. Methods Biomech. Biomed. Eng.* **16**, 530–543. (doi:10.1080/10255842.2011.628448)
43. Gzaiel M, Triki E, Barkaoui A. 2019 Finite element modeling of the puncture-cutting response of soft material by a pointed blade. *Mech. Mater.* **136**, 103082. (doi:10.1016/j.mechmat.2019.103082)
44. Mohammadi H, Ebrahimian A, Maftoon N. 2021 Fracture behaviour of human skin in deep needle insertion can be captured using validated cohesive zone finite-element method. *Comput. Biol. Med.* **139**, 104982. (doi:10.1016/j.compbiomed.2021.104982)
45. Horgan C, Smayda M. 2012 The trousers test for tearing of soft biomaterials. *Int. J. Solids Struct.* **49**, 161–169. (doi:10.1016/j.ijsolstr.2011.09.018)
46. Joodaki H, Panzer M. 2018 Skin mechanical properties and modeling: a review. *Proc. Inst. Mech. Eng. H* **232**, 323–343. (doi:10.1177/0954411918759801)
47. Diani J. 2001 Irreversible growth of a spherical cavity in rubber-like material: a fracture mechanics description. *Int. J. Fract.* **112**, 151–161. (doi:10.1023/A:1013311526076)
48. Cho W *et al.* 2012 Microstructured barbs on the North American porcupine quill enable easy tissue penetration and difficult removal. *Proc. Natl Acad. Sci. USA* **109**, 21 289–21 294. (doi:10.1073/pnas.1216441109)
49. Clark D, Hauber M, Anderson P. 2021 Nest substrate and tool shape significantly affect the mechanics and energy requirements of avian eggshell puncture. *J. Exp. Biol.* **224**, jeb238832. (doi:10.1242/jeb.238832)

50. Evans A, Sanson G. 1998 The effect of tooth shape on the breakdown of insects. *J. Zool.* **246**, 391–400. (doi:10.1111/j.1469-7998.1998.tb00171.x)
51. Zhang B, Shiang C, Yang S, Hutchens S. 2019 Y-shaped cutting for the systematic characterization of cutting and tearing. *Exp. Mech.* **59**, 517–529. (doi:10.1007/s11340-019-00479-2)
52. Higham T *et al.* 2021 Linking ecomechanical models and functional traits to understand phenotypic diversity. *Trends Ecol. Evol.* **36**, 860–873. (doi:10.1016/j.tree.2021.05.009)
53. Pollock T, Hocking D, Evans A. 2021 The killer's toolkit: remarkable adaptations in the canine teeth of mammalian carnivores. *Zool. J. Linn. Soc.*, 1–18. (doi:10.1093/zoolinnean/zlab064)
54. Evans A, Hunter J, Fortelius M, Sanson G, Evans A, Hunter J. 2005 The scaling of tooth sharpness in mammals. *Ann. Zool. Fennici* **42**, 603–613.
55. Mahvash M, Dupont P. 2009 Fast needle insertion to minimize tissue deformation and damage. In *2009 IEEE Int. Conf. on Robotics and Automation, Kobe, Japan, 12–17 May,* pp. 3097–3102. IEEE. (doi:10.1109/ROBOT.2009.5152617)
56. Atkins T. 2009 Sharpness and bluntness: absolute or relative? In *The science and engineering of cutting*, pp. 221–243. Oxford, UK: Butterworth-Heinemann, Elsevier.
57. Wang Y, Tai B, Yu H, Shih A. 2014 Silicone-based tissue-mimicking phantom for needle insertion simulation. *J. Med. Devices* **8**, 1–7. (doi:10.1115/1.4026508)
58. Bao X, Li W, Lu M, Zhou Z. 2016 Experiment study on puncture force between MIS suture needle and soft tissue. *Biosurface Biotribol.* **2**, 49–58. (doi:10.1016/j.bsbt.2016.05.001)
59. Lucas P. 2004 Tooth shape. In *Dental functional morphology: how teeth work*, pp. 87–132. Cambridge, UK: Cambridge University Press.
60. Aoyagi S, Izumi H, Fukuda M. 2008 Biodegradable polymer needle with various tip angles and consideration on insertion mechanism of mosquito's proboscis. *Sens. Actuators, A* **143**, 20–28. (doi:10.1016/j.sna.2007.06.007)
61. Malandrino A, Moeendarbary E. 2019 Poroelasticity of living tissues. In *Encyclopedia of biomedical engineering* (ed. R Narayan), pp. 238–245. Amsterdam, The Netherlands: Elsevier.
62. Jiang H, Browning R, Fincher J, Gasbarro A, Jones S, Sue H. 2008 Influence of surface roughness and contact load on friction coefficient and scratch behavior of thermoplastic olefins. *Appl. Surf. Sci.* **254**, 4494–4499. (doi:10.1016/j.apsusc.2008.01.067)
63. Persson B, Albohr O, Tartaglino U, Volokitin A, Tosatti E. 2005 On the nature of surface roughness with application to contact mechanics, sealing, rubber friction and adhesion. *J. Phys.: Condens. Matter* **17**, R1–R62. (doi:10.1088/0953-8984/17/1/R01)
64. Popowics T, Fortelius M. 1997 On the cutting edge: tooth blade sharpness in herbivorous and faunivorous mammals. *Ann. Zool. Fennici* **34**, 73–88.
65. Meij M, Bout R. 2004 Scaling of jaw muscle size and maximal bite force in finches. *J. Exp. Biol.* **207**, 2745–2753. (doi:10.1242/jeb.01091)
66. Copes L, Schwartz G. 2010 The scale of it all: postcanine tooth size, the taxon-level effect, and the universality of Gould's scaling law. *Paleobiology* **36**, 188–203. (doi:10.1666/08089.1)
67. Evans A, Sanson G. 2005 Correspondence between tooth shape and dietary biomechanical properties in insectivorous microchiropterans. *Evol. Ecol. Res.* **7**, 453–478.
68. Rosario M, Sutton G, Patek S, Sawicki G. 2016 Muscle-spring dynamics in time-limited, elastic movements. *Proc. R. Soc. B* **283**, 20161561. (doi:10.1098/rspb.2016.1561)
69. Gutstein W. 1956 A generalization of Hooke's law in muscle elasticity. *Bull. Math. Biophys.* **18**, 151–170. (doi:10.1007/BF02477838)
70. Chintapalli R, Breton S, Dastjerdi A, Barthelat F. 2014 Strain rate hardening: a hidden but critical mechanism for biological composites? *Acta Biomater.* **10**, 5064–5073. (doi:10.1016/j.actbio.2014.08.027)
71. Zhang B, Anderson PSL. 2022 Modelling biological puncture: a mathematical framework for determining the energetics and scaling. Figshare. (doi:10.6084/m9.figshare.c.6238488)